Research article

Bakhtiyar Orazbayev and Romain Fleury*

Quantitative robustness analysis of topological edge modes in C6 and valley-Hall metamaterial waveguides

https://doi.org/10.1515/nanoph-2019-0137
Received May 7, 2019; accepted June 20, 2019

Abstract: Recent advances in designing time-reversal-invariant photonic topological insulators have been extended down to the deep subwavelength scale, by employing synthetic photonic matter made of dense periodic arrangements of subwavelength resonant scatterers. Interestingly, such topological metamaterial crystals support edge states that are localized in subwavelength volumes at topological boundaries, providing a unique way to design subwavelength waveguides based on engineering the topology of bulk metamaterial insulators. While the existence of these edge modes is guaranteed by topology, their robustness to backscattering is often incomplete, as time-reversed photonic modes can always be coupled to each other by virtue of reciprocity. Unlike electronic spins which are protected by Kramers theorem, photonic spins are mostly protected by weaker symmetries like crystal symmetries or valley conservation. In this paper, we quantitatively studied the robustness of subwavelength edge modes originating from two frequently used topological designs, namely metamaterial spin-Hall (SP) effect based on C6 symmetry, and metamaterial valley-Hall (VH) insulators based on valley preservation. For the first time, robustness is evaluated for position and frequency disorder and for all possible interface types, by performing ensemble average of the edge mode transmission through many random realizations of disorder. In contrast to our results in the previous study on the chiral metamaterial waveguide, the statistical study presented here demonstrates the importance of the specific interface on the robustness of these edge modes and the superior robustness of the VH edge stated in both position and frequency disorder, provided one works with a zigzag interface.

Keywords: topological insulators; valley transport; Anderson localization; symmetry protection.

***Corresponding author: Romain Fleury,** Laboratory of Wave Engineering, École Polytechnique Fédérale de Lausanne (EPFL), 1015 Lausanne, Switzerland, e-mail: romain.fleury@epfl.ch.
https://orcid.org/0000-0002-9486-6854
Bakhtiyar Orazbayev: Laboratory of Wave Engineering, École Polytechnique Fédérale de Lausanne (EPFL), 1015 Lausanne, Switzerland

1 Introduction

The recent progress in the field of photonic topological insulators (TIs) has led to the discovery of several schemes of inducing edge states at topological interfaces between photonic insulators [1–9]. Not only the presence of edge modes is guaranteed by the topology of the surrounding bulk insulators, but also in some cases the edge modes are immune to backscattering even when defects are present along the interface, such as geometrical disorder or interface bends [1–20]. This is always the case for Chern insulators, a class of photonic insulators whose topology relies on time-reversal symmetry breaking, and induces non-reciprocal unidirectional transport on the topological boundary [6, 20, 21]. Conversely, immunity to backscattering is not a priori true for designs that preserve time-reversal symmetry, in which reciprocity necessarily holds implying that every edge mode always comes with its time-reversed image [1, 4, 5, 7, 22, 23]. In these time-reversal invariant cases, the question of robustness boils down to whether the two time-reversed states (often called photonic pseudo-spins) can be coupled to each other by the considered defect. In the literature, the two dominant time-reversal invariant topological designs, namely, spin-Hall (SP) designs based on six-fold rotational symmetry (C6) [8, 22, 23] and VH designs based on valley preservation [5, 18, 24, 25], have often been claimed as topologically protected, although they are not strictly immune to backscattering. The real level of robustness of the edge modes originating from these designs has been left largely unexplored, limited to field maps without any quantitative analysis and/or simulations for a specific realization of disorder.

Here, we report a quantitative assessment of the level of robustness of time-reversal invariant topological edge modes, based on a clearly defined universal metric: the Anderson localization length [26–28] of the mode along the topological interface [29]. Such a length is numerically computed by taking ensemble averages of the transmission coefficient through a disordered region of variable length along the interface, for many realizations of disorder [30]. This allows us to rigorously quantify and compare the robustness of C6 and VH edge modes to disorders of different possible types of interfaces.

We want to stress here that we have chosen to focus on topological insulators of a special type, i.e. based on locally resonant metamaterial crystals [31, 32]. These artificial materials are built from spatially local subwavelength resonant scattering inclusions (e.g. electrically small resonant dipoles), which are arranged periodically at a subwavelength scale, leading to deeply subwavelength edge modes [33]. The reason for this choice is that such compact systems are of large practical importance to manipulate electromagnetic waves along the subwavelength paths (from microwave engineering to plasmonics), however such slow-light propagation is usually particularly sensitive to defects and disorder. In this regime, other types of slow-light waveguides which are not based on topology have been demonstrated and their robustness is quantitatively explored, which allows us to not only to compare topological designs between each other, but also to determine whether their topological origin provides them with a superior robustness with respect to conventional designs, like the ones based on defect-lines [33] or chirality [30].

The paper is structured in to following Sections: Section 2, we have briefly described the designs of C6-based and VH-based metamaterial TIs along with the existence of topological edge modes between different interfaces. We have defined different kinds of disorder that can be introduced at such interfaces and define the basis of our statistical study. In Section 3, we have presented the obtained results for all types of interfaces and disorders. Finally, in Section 4, we have discussed how different disorders affect the transmission efficiency and how important the type of interface is, for the robustness of the waveguide.

2 Materials and methods

The schematics of the C6 and VH metamaterial TIs studied in this work are shown in Figure 1A and B, respectively where the colored disks represent the spatially local resonators composing the metamaterial crystals. These resonators are assumed here to be quarter-wavelength copper rods standing on a ground plane and oriented along z (the figure view is from the top), corresponding to a microwave implementation of locally resonant metamaterials, whose structure is effectively subwavelength in the xOy plane. This specific microwave implementation does not impact the generality of our study, since similar dispersion curves and topological behavior are obtained as long as one considers 2D arrangements of far-field coupled dipolar resonances [33], which can also be obtained at optical frequencies (with dielectric or plasmonic resonators), or in other physical platforms, like acoustics [34] or elastodynamics [35].

First, we started with designing a C6 TI from the usual procedure [8, 22], i.e. by considering a honeycomb lattice of resonators (in red in Figure 1A), separated by a distance $c=0.125\lambda_0$, where λ_0 is the operating wavelength. Instead of looking at this lattice using a primitive rhombic unit cell with two resonators, we follow Ref. [8] and consider an extended unit cell containing six-resonators (dashed lines), viewing the honeycomb lattice as a triangular lattice of hexagonal units (with a period $a=3c$) (see Figure 1A). Therefore, as demonstrated in previous works [8, 22], by expanding (shrinking) this hexagonal cluster of resonators, thereby preserving the six-fold rotational (C6) symmetry of the lattice, it is possible to open a complete topological (trivial) band gap. This band gap is highlighted in orange in the band structures computed using the finite element method (FEM) which are represented in the bottom panel of Figure 1A for the cases $3c/a=0.8$ (red dots, shrunken hexagons), and $3c/a=1.2$ (blue dots, expanded hexagons). The well-known distinct topological nature of the metamaterial insulators with expanded and shrunken hexagonal clusters [8, 22] will be exploited in the following to form topological edge modes at an interface between these two media.

Second, we have also designed a VH metamaterial TI by starting again from a hexagonal lattice of resonators of equal resonance frequencies (i.e. equal height, in blue), and open a band gap by detuning the two resonators within the unit cell, increasing the first resonance frequency by a factor $1+\beta$ (yellow disks) and decreasing the second by a factor $1-\beta$ (orange disks), i.e. $f_{1,2}=(1\pm\beta)f_c$. Being time-reversed of each other, the two valleys of this insulator at K and K' have opposite Berry curvatures, implying the existence of an edge mode at the interface between a crystal with opposite signs of the inversion symmetry breaking parameter β [we have referred them as type A ($f_1<f_2$) and B ($f_2>f_1$)] [5, 36]. This mechanism will form the basis of the emergence of VH edge modes in the following.

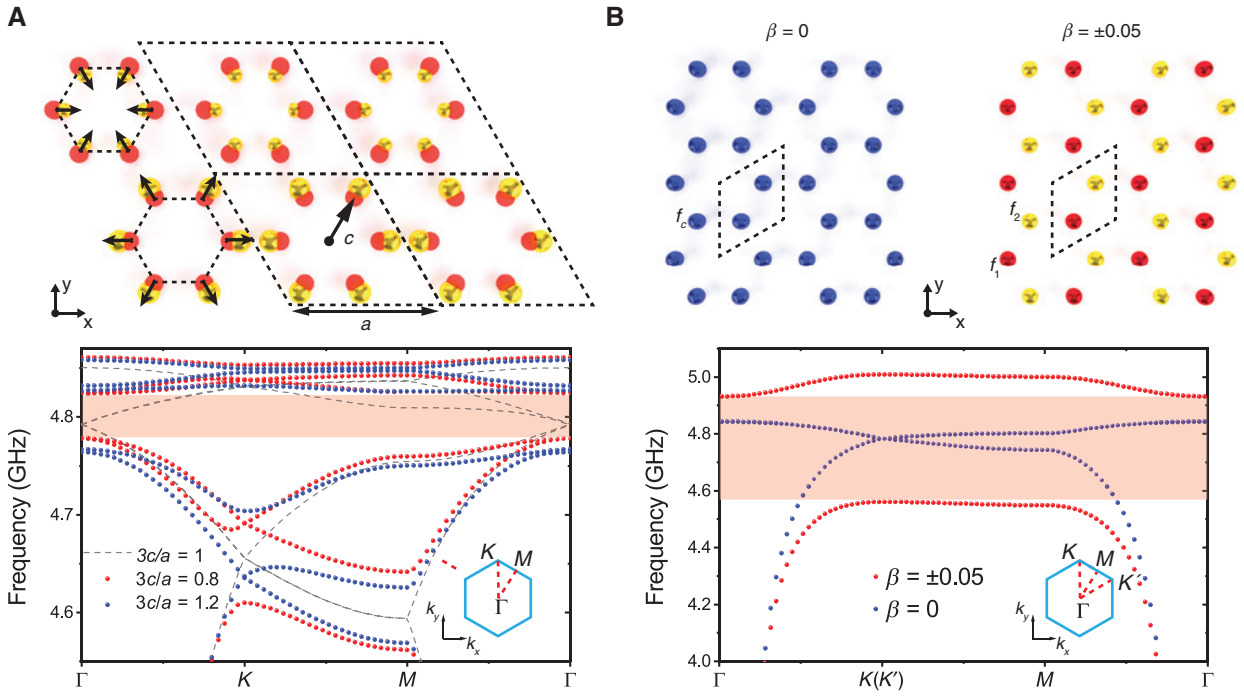

Figure 1: The schematics and corresponding numerical band structures for metamaterial topological insulators (TIs) considered in this work. Metamaterial TI based on (A) C6 symmetry and (B) valley conservation. In the top panels, the colored disks represent the spatially local resonators composing the metamaterial crystals. These resonators are assumed to be quarter-wavelength copper rods standing on a ground plane and oriented along z (the figure view is from the top), corresponding to a microwave implementation of local resonant metamaterials, whose structure is effectively subwavelength in the *xOy* plane. The bottom panels represent the associated numerical band structures obtained from full-wave numerical simulations.

Next, we defined the possible interfaces for both C6-based and VH waveguides. For the first waveguide (C6), there are two possible interfaces: armchair and zigzag, as shown in the top panels of Figure 2A and B. In the bottom panels, we represent the dispersion of the edge modes propagating along the interface (red bands) within the band gap left by the bulk modes (grey). Importantly, the presence of the interface itself already breaks the C6 symmetry of the system, which implies that time-reversed topological edge modes can interact with each other and are gapped near Γ (panel A, bottom). As already known, in case of zigzag interface, the breaking of symmetry is less important [37] and the minigap closes almost completely (see Figure 2B). Note the appearance of a third flat band in panel B, which is unimportant for our purpose as it corresponds to a trivial edge mode that depends on this specific microwave implementation.

For the VH waveguide there are three possible interfaces: bridge (Figure 2C), armchair (Figure 2D) and zigzag (Figure 2E). In the case of the bridge and zigzag interfaces, there exist an additional two possible connections, depending on whether the interface is taken next to the low-frequency resonators or the high frequency ones: A-B and B-A. For the bridge interface both interconnections give the same valley-protected edge modes (see Figure 2C), while for the zigzag interface B-A, the edge dispersion occurs at a lower frequency than A-B (see Figure 2D). Note, only the bridge and zigzag interface point in the direction Γ*K*, and therefore are consistent with the VH conservation scheme. The armchair interface, which goes along Γ*M*, is not expected to support particularly robust edge states, since they are constructed away from the *K* and *K*′ valleys. In the following Section 3, we have rigorously proved that it is the case.

Having introduced the two metamaterial crystals and their interfaces, we move forward to the study of their robustness against different sorts of disorder, which are defined in Figure 3. The first type is a position disorder, which we represent in Figure 3A for the bridge valley interface and corresponds to random shifts in the position of the resonators in any direction and in the range $[0, R_{def}]$, resulting in a local rupture of the lattice symmetry. In the second type of disorder (Figure 3A), the resonators are not moved, but their resonance frequencies are shifted by a random value in the range $[-\delta f, \delta f]$, also affecting the

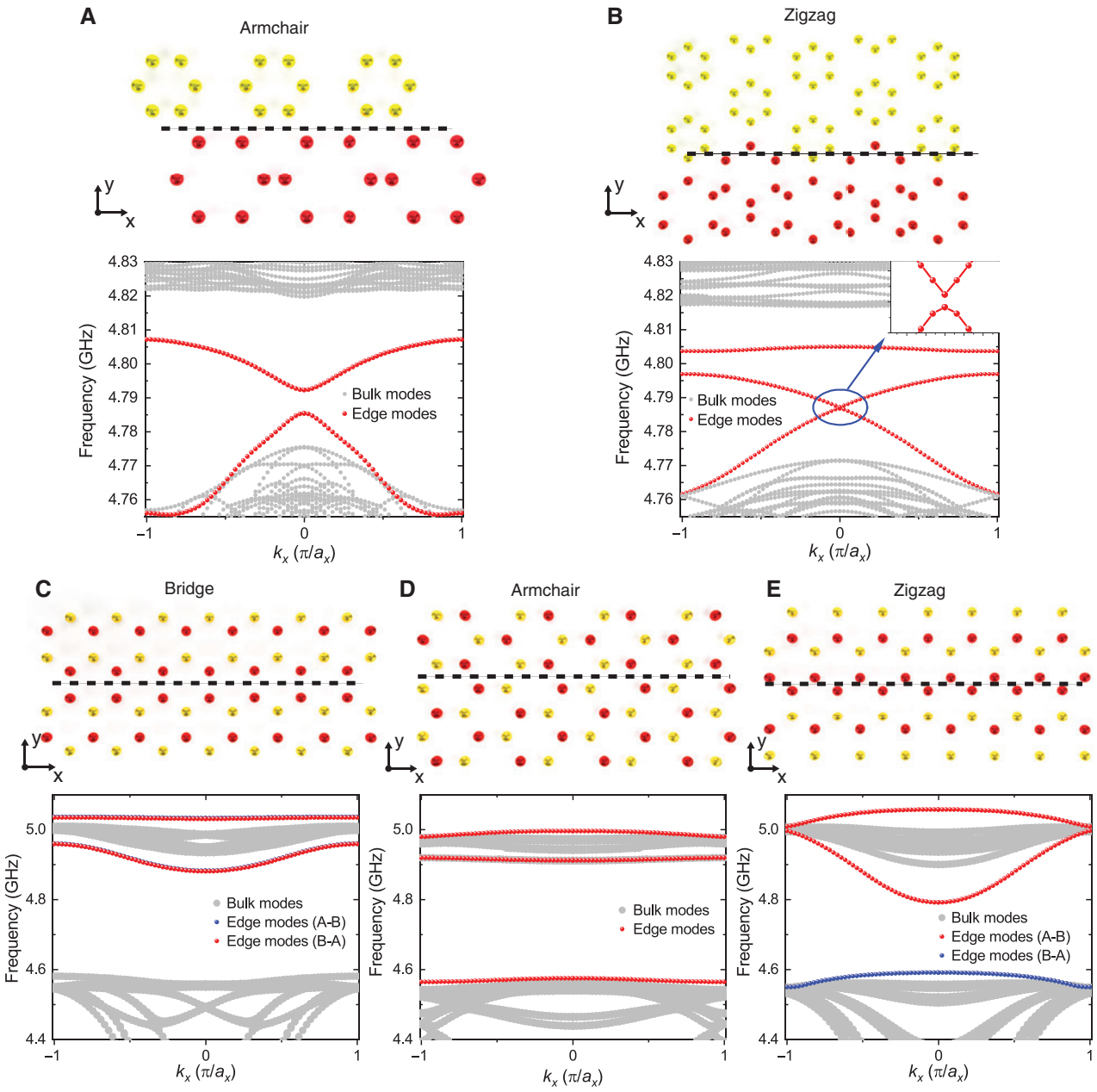

Figure 2: Possible interfaces and associated edge mode dispersions between C6-based and VH-based metamaterial TIs.
(A) Armchair and (B) zigzag interfaces for the C6-based edge modes, (C) bridge, (D) armchair and (E) zigzag interfaces for VH-based edge modes. The bulk modes are shown in grey, and the edge modes in blue and red, depending on the sign of β.

local periodicity of the interface. Both types of defects can lead to backscattering, since they either increase the breaking of C6-symmetry or potentially induce intervalley-coupling. Finally, we also considered the typical sharp turn (Figure 3C) often seen in papers about VH insulators, in which an edge mode propagating along ΓK_1 is routed towards ΓK_2.

Let us first discuss the cases of position and frequency disorders, whose effect on the edge mode propagation requires a statistical approach, in order to average their quantitative behavior out of an ensemble of realizations of disorder. In order to carry on statistical studies, we resorted to a semi-analytical model based on coupled two-dimensional dipoles [38], with the advantage of faster computing times with respect to three-dimensional FEM simulations [22]. In such model, the resonant inclusions are modeled as dipoles with electrical polarizabilities and coupled to each other through the 2D free-space Green's functions (see Supplementary material for more details). This semi-analytical code was checked to be consistent

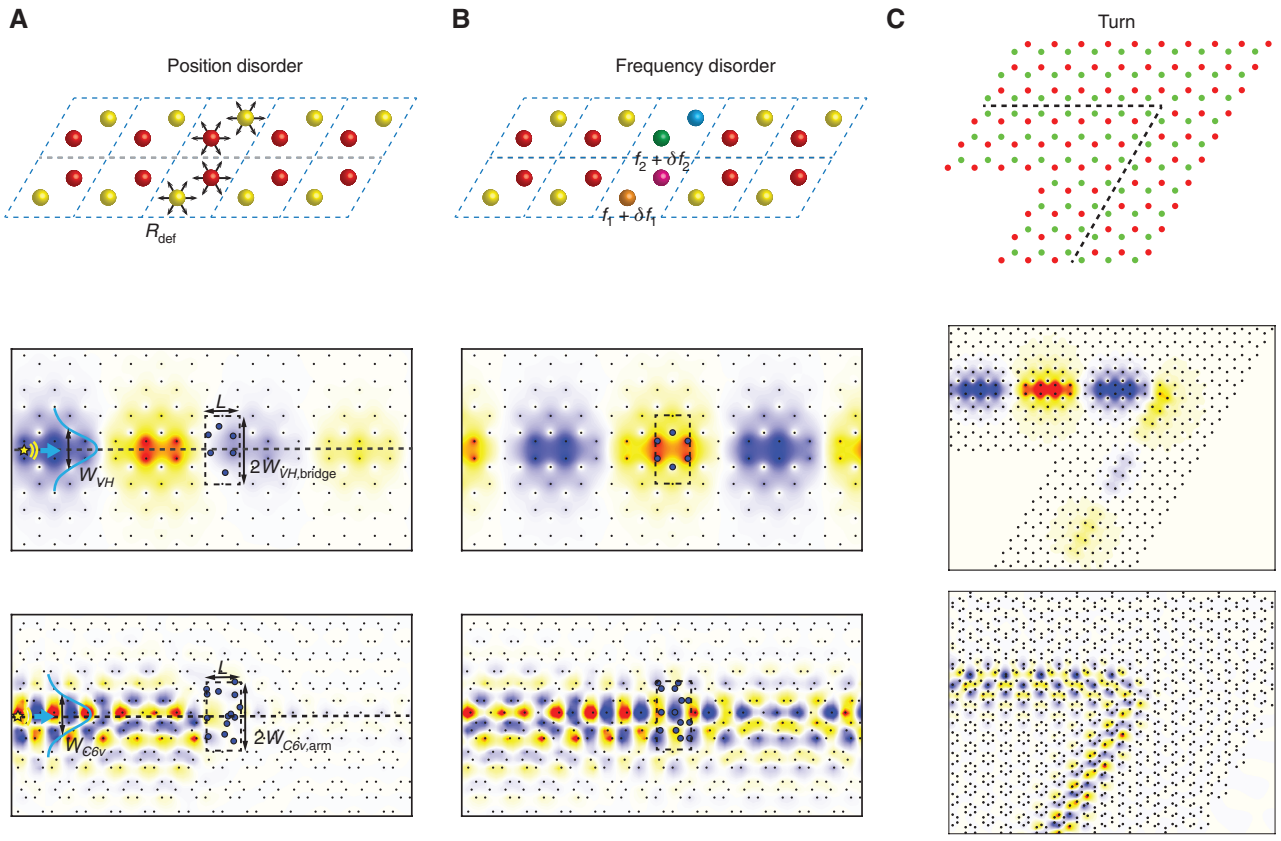

Figure 3: Different types of disorders and obstacles studied in this work.
(A) Position and (B) frequency disorder (top panels) are introduced by displacing the resonators or changing their resonance frequency. The disorders are contained in a box of size $2W \times L$ along the interface, where W is the transverse mode width and L is the varying length of the box. Each resonator within this box is affected by a random disorder in the range $[0, R_{def}]$ for position and $[-\delta f, \delta f]$ for frequency disorders. (C) Another type of obstacle is a sharp turn (top panel) and corresponding electric field distributions for VH metamaterial TI with bridge interface (middle panel) and C6 metamaterial TI with zigzag interface (bottom panel), respectively. The electric field color maps in (A) and (B) are generated for a box length $L = W$ and disorder strengths in the range of $R_{def} = [0, 0.2W]$, $\delta f = [-BW, BW]$, for position and frequency disorders, respectively (BW is the bandwidth of the transmission band for each waveguide).

with the full three-dimensional case in terms of mode profiles and dispersion (examples of semi-analytical mode profiles for particular interfaces are shown in the bottom panels of Figure 3). Similar to our previous work [30], this technique allowed us to extract the transmission coefficient S_{21} of an edge mode through a disorder box of length L along the interface (the width of the box is set to twice the mode width at half intensity maximum W). For a given length we evaluated the transmission coefficient (S_{21}) as a function of disorder strength in case of position [frequency] disorder $S_{21}(R_{def})[S_{21}(\delta f)]$, and averaged it over many realizations of disorder, keeping the strength of the disorder constant. In order to treat edge modes with different localization and group velocity on an equal footing, the ratio $\tilde{R}_{def} = R_{def} / W_{C6,VH}$ for position defects and $\delta\tilde{f} = \delta f / BW_{C6,VH}$ for frequency defects is fixed (where $W_{c6,VH}$ is the mode width at half intensity maximum and $BW_{C6,VH}$ is the bandwidth of the transmission band for C6 and VH waveguides, respectively). It is important to stress that, unlike the technique used in our previous work on a chiral metamaterial waveguide [30], this technique is applied to different possible interfaces between the TIs while ensuring a fair comparison between these different systems. We also stress that the frequency at which this study is performed on the edge mode band is carefully chosen to be the one where the transmission is the most robust, which is near Γ for the C6 design, and near K for the VH design. In case of the sharp turn, we do not need to perform statistical averages and simply analyze the transmission coefficient (S_{21}) as a function of operating frequency $S_{21}(f)$ in case of the different interfaces. Examples of such sharp curved waveguides for valley (bridge interface) and C6-symmetry (zigzag interface) with semi-analytical color maps of the electric field distribution are shown in Figure 3C (middle and bottom panels), and other cases in the Supplementary material.

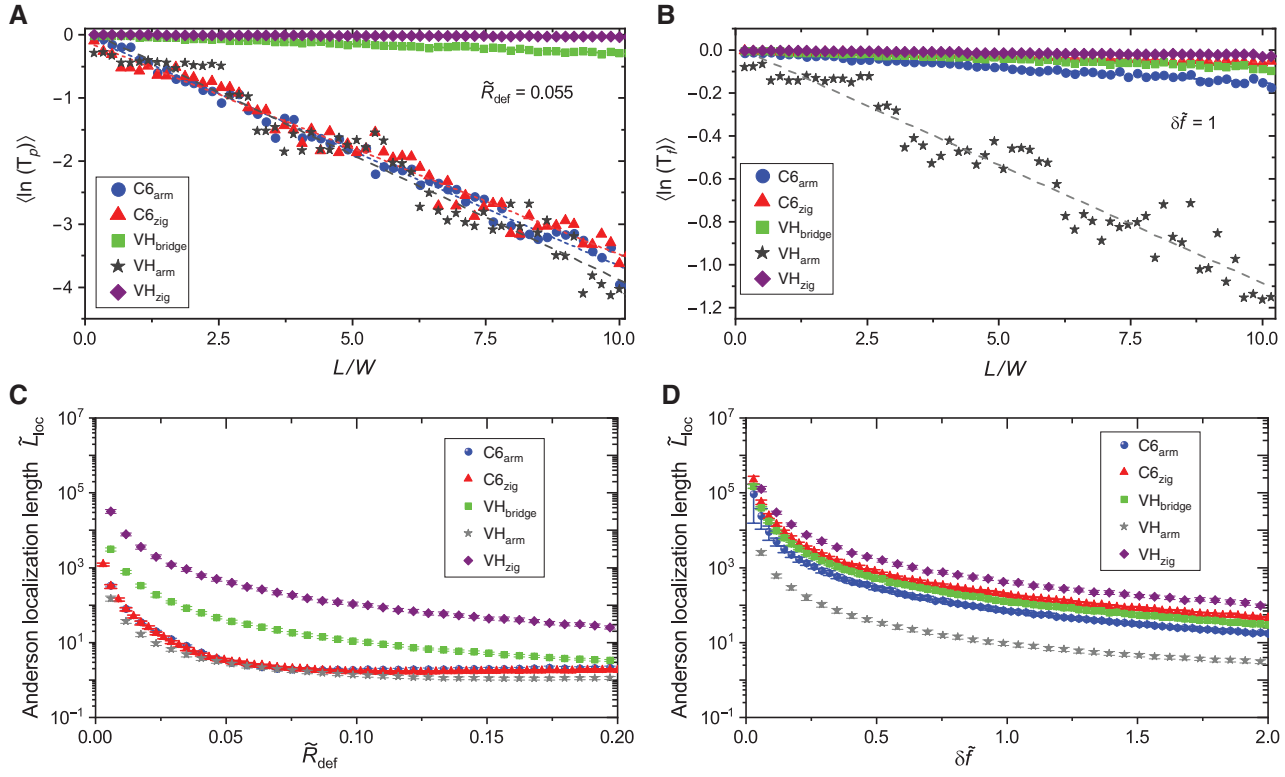

Figure 4: Statistical analysis of the robustness of topological subwavelength-guiding systems in the presence of position and frequency disorder: the C6-based waveguides with armchair (blue circles) and zigzag (red triangles) interfaces, VH-based waveguides with bridge (green squares), armchair (gray stars) and zigzag (purple rhombs) interfaces.
Ensemble average logarithm of the numerically obtained transmission $\langle \ln(T_{p,f}) \rangle$ as a function of the disorder box length L for (A) position (with normalized strength $\tilde{R}_{def} = 0.055$) and (B) frequency (with normalized strength $\delta\tilde{f} = 1$) disorders. Normalized Anderson localization length ($\tilde{L}_{loc} = -(L/W)/\langle \ln(T_{p,f}) \rangle$) as a function of the normalized amplitude of (C) position ($\tilde{R}_{def}$) and (D) frequency ($\delta\tilde{f}$) disorders. Each point represents an inverse of the slope $\langle \ln(T_{p,f}) \rangle$ as a function of the disorder box length L shown in (A) and (B). The vertical error bars represent the standard deviation of $\tilde{L}_{loc}$ for each disorder amplitude (they are barely visible).

3 Results

The transmission efficiency (S_{21}) of each waveguide geometry averaged over 150 different realizations of disorders for all possible interfaces is represented in Figure 4A and B, assuming a fixed disorder strength $\tilde{R}_{def} = 0.055$ and $\delta\tilde{f} = 1$, while varying the defect box length L. In these figures, we do not represent directly the average of the magnitude of S_{21}, but instead the average of its logarithm as a function of L. They are denoted as $\langle \ln(T_p) \rangle$ and $\langle \ln(T_f) \rangle$ for disorders in the position and frequency, respectively. From the figure it is clear that the different waveguides are not equivalent, with some designs handling much better presence of disorder as the length L gets larger. One can also clearly observe that the average logarithms $\langle \ln(T_p) \rangle$, $\langle \ln(T_f) \rangle$ computed for fixed strengths of disorder (R_{def}, δf = const) drop linearly with the increasing length of the disorder box L, which is a clear sign of 1D Anderson localization [26, 39].

Thus, as a quantitative metric, we can calculate the normalized Anderson localization length $\tilde{L}_{loc} = -(L/W)/\langle \ln(T_{p,f}) \rangle$ by extracting the inverse slopes of the curves of Figure 4A and B, and repeat this operation for other values of R_{def} and δf. The obtained normalized Anderson localization length $\tilde{L}_{loc}$ for each guiding system and each type of disorder are shown in Figure 4C–D as a function of the disorder strength. From these figures, it can be observed that the robustness of the propagating edge waves strongly depends on the geometry and on the type of interface. For instance, consistent with results previously obtained in Ref. [30], the robustness of the C6-based armchair interface is poor when it comes to position disorder, resulting in a quick drop of $\tilde{L}_{loc}$ below $10W$ for disorder strength as low as 5% of W. The VH-based armchair interface, which is aligned in the "wrong" direction (namely ΓM), is very weak to both position and frequency disorders. The VH-based zigzag interface mode is instead quite robust to both disorder types. C6-based

interfaces are not very robust to position disorder, since they inherently break C6 symmetry; however their performance in terms of frequency robustness is equivalent to most other designs.

Finally, we move to the study of the turns. We obtained the transmission coefficient as a function of operating frequency $S_{21}(f)$ in the presence of the sharp turns along the propagation path for all waveguides. Due to C_{3v}- and C_{6v}-symmetries of the unit cells, the propagation path can be curved with a limited number of angles (namely 60° steps). Here, for the sake of simplicity the transmission is analyzed only for a 120° turn, which respects the valley polarization and is compatible with all the C6-based interfaces. We discard the other possibilities which are known to transmit very poorly in the VH case. The extracted semi-analytical S parameters for all interfaces of C6- and VH-based waveguides are shown in Figure 5A–E.

For the armchair interface of the C6-based waveguide (Figure 5A), the higher frequency band has two transparency windows of transmission, while the transmission drops to zero around Γ point (this corresponds to the point close to the minigap in the band structure of Figure 2A). In the zigzag interface of the C6-based waveguide (Figure 5B), the transparency window is now located next to the minigap or around Γ point, which is consistent with previous observations [37]. In the case of the VH-based waveguides, none of the interfaces provide a total transmission within the analyzed frequency bands. Moreover, as expected of such designs, the transmission drops to zero around Γ point and increases near K points (see Figure 5C–E).

4 Discussion

The quantitative study presented in this work clearly demonstrates that time-reversal invariant metamaterial topological insulators can be used to induce an interesting class of subwavelength topological edge modes, possess a degree of robustness that in the best case, only slightly outperforms that of other subwavelength slow-waveguides based on other means [33]. Under no circumstances, they can provide total immunity against backscattering, as it is the case of Chern topological insulators, as one can sometimes read in prior arts. The most robust of all the designs explored here is the VH-based zigzag interface, which possesses the unique property of being significantly robust to both position and frequency disorder. Similar performance has already been reported with a different subwavelength waveguide design, based on chirality [30, 40]. The other waveguiding schemes compared in this work demonstrate a certain level of protection, stronger for either position or frequency disorder (see Figure 4C and D), which can be explained by the

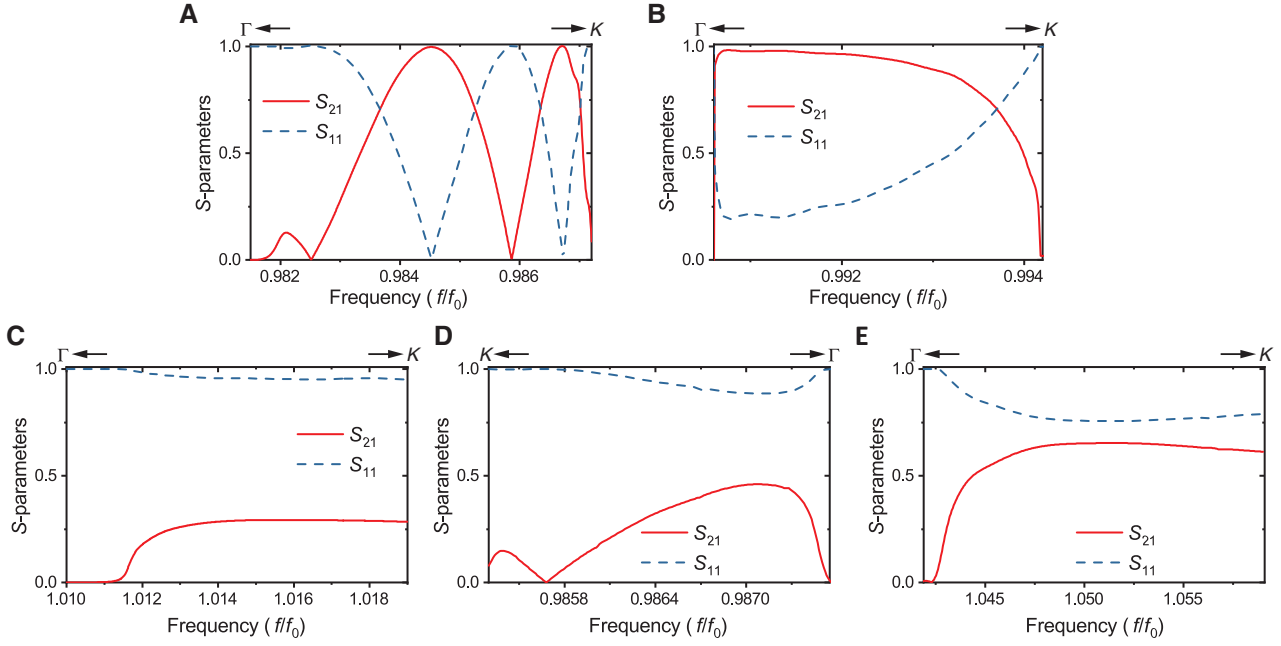

Figure 5: The extracted S parameters for the 60 degrees sharp turn.
Spectrum for (A) the armchair and (B) zigzag interfaces of the C6-symmetry-based waveguide, (C) bridge, (D) armchair and (E) zigzag interface of the VH-based PTI waveguide. The extracted S_{11} parameters are represented with blue dashed lines and S_{21} with red solid lines.

physical symmetries underlying the topological protection. In the C6-based waveguides, any random displacements of the resonators will locally break the symmetry of the hexagonal clusters, mixing the two pseudospin states and reducing the Anderson localization length for both armchair and zigzag interfaces (blue spheres and red triangles, respectively in Figure 4A). However, by introducing a zigzag interface, which reduces the minigap between the edge mode bands [37], these modes are less affected by the lattice disorders. In case of frequency disorders, the C6-based design is less affected by the local changes in the resonance frequency of resonators, which results in a more robust behavior (blue spheres and red triangles, respectively in Figure 4B). In the VH-based waveguides, the direction of the interface is very important, and the edge mode is poorly robust in any direction other than Γ*K*. Finally, the study of a turn demonstrates the importance of quantitative metrics for the evaluation of topological robustness, highlighting a largely incomplete degree of robustness that depends on frequency, and on the specific design, despite the fact that all these designs are often reported as "topologically protected".

To summarize, we have performed a statistical study that quantifies with a clear universal metric the robustness to disorder of two different types of waveguiding systems based on time-reversal invariant metamaterial topological insulators, namely systems based on six-fold crystalline symmetry and valley conservation. The obtained results have demonstrated the importance of quantitative metrics for the study and discussion of topological protection and related properties, and highlighted the good performance of the zigzag interface of VH metamaterial insulators when compared to the existing literature. We want to stress here that the study focused on locally resonant periodic metamaterials that are based on periodic arrangements of subwavelength resonators, interacting via multiple scattering, and Fano interferences [41]. A possible extension of this work is to consider whether our conclusions still hold in the case of non-resonant photonic crystals which are based on different physics, namely Bragg interferences. We believe that such systematic quantitative robustness study is an indispensable tool for the practical realization of disruptive subwavelength-guiding systems that are robust to fabrication tolerances and external factors, not only at microwaves, but also for plasmonics or in the area of dielectric-based nanophotonics.

Acknowledgments: This work was supported by the Swiss National Science Foundation (SNSF) under Grant No. 172487.

References

[1] Hafezi M, Demler EA, Lukin MD, Taylor JM. Robust optical delay lines with topological protection. Nat Phys 2011;7:907–12.
[2] Rechtsman MC, Zeuner JM, Plotnik Y, et al. Photonic floquet topological insulators. Nature 2013;496:196–200.
[3] Cheng X, Jouvaud C, Ni X, Mousavi SH, Genack AZ, Khanikaev AB. Robust reconfigurable electromagnetic pathways within a photonic topological insulator. Nat Mater 2016;15:542–8.
[4] Gao F, Gao Z, Shi X, et al. Probing topological protection using a designer surface plasmon structure. Nat Commun 2016;7:11619.
[5] Ma T, Shvets G. All-Si valley-Hall photonic topological insulator. New J Phys 2016;18:025012.
[6] Wang Z, Chong Y, Joannopoulos JD, Soljacić M. Observation of unidirectional backscattering-immune topological electromagnetic states. Nature 2009;461:772–5.
[7] Hafezi M, Mittal S, Fan J, Migdall A, Taylor JM. Imaging topological edge states in silicon photonics. Nat Photonics 2013;7:1001–5.
[8] Wu L-H, Hu X. Scheme for achieving a topological photonic crystal by using dielectric material. Phys Rev Lett 2015;114:223901.
[9] Khanikaev AB, Mousavi SH, Tse W-K, Kargarian M, MacDonald AH, Shvets G. Photonic topological insulators. Nat Mater 2013;12:233–9.
[10] Poo Y, Wu RX, Lin Z, Yang Y, Chan CT. Experimental realization of self-guiding unidirectional electromagnetic edge states. Phys Rev Lett 2011;106:12011.
[11] Lu L, Fang C, Fu L, Johnson SG, Joannopoulos JD, Soljačić M. Symmetry-protected topological photonic crystal in three dimensions. Nat Phys 2016;12:337–40.
[12] Chen W-J, Jiang S-J, Chen X-D, et al. Experimental realization of photonic topological insulator in a uniaxial metacrystal waveguide. Nat Commun 2014;5:5782.
[13] Lai K, Ma T, Bo X, Anlage S, Shvets G. Experimental realization of a reflections-free compact delay line based on a photonic topological insulator. Sci Rep 2016;6:28453.
[14] Xiao B, Lai K, Yu Y, Ma T, Shvets G, Anlage SM. Exciting reflectionless unidirectional edge modes in a reciprocal photonic topological insulator medium. Phys Rev B 2016;94:195427.
[15] Slobozhanyuk AP, Khanikaev AB, Filonov DS, Smirnova DA, Miroshnichenko AE, Kivshar YS. Experimental demonstration of topological effects in bianisotropic metamaterials. Sci Rep 2016;6:22270.
[16] Ma T, Khanikaev AB, Mousavi SH, Shvets G. Guiding electromagnetic waves around sharp corners: topologically protected photonic transport in metawaveguides. Phys Rev Lett 2015;114:127401.
[17] Mittal S, Fan J, Faez S, Migdall A, Taylor JM, Hafezi M. Topologically robust transport of photons in a synthetic gauge field. Phys Rev Lett 2014;113:087403.
[18] Ma T, Shvets G. Scattering-free edge states between heterogeneous photonic topological insulators. Phys Rev B 2017;95:165102.
[19] Chen XD, Zhao FL, Chen M, Dong JW. Valley-contrasting physics in all-dielectric photonic crystals: orbital angular momentum and topological propagation. Phys Rev B 2017;96:020202(R).

[20] Wang Z, Chong YD, Joannopoulos JD, Soljačić M. Reflection-free one-way edge modes in a gyromagnetic photonic crystal. Phys Rev Lett 2008;100:013905.
[21] Raghu S, Haldane FDM. Analogs of quantum-hall-effect edge states in photonic crystals. Phys Rev A – At Mol Opt Phys 2008;78:033834.
[22] Yves S, Fleury R, Berthelot T, Fink M, Lemoult F, Lerosey G. Crystalline metamaterials for topological properties at subwavelength scales. Nat Commun 2017;8:16023.
[23] Yang Y, Xu YF, Xu T, et al. Visualization of a unidirectional electromagnetic waveguide using topological photonic crystals made of dielectric materials. Phys Rev Lett 2018;120:217401.
[24] Noh J, Huang S, Chen KP, Rechtsman MC. Observation of photonic topological valley Hall edge states. Phys Rev Lett 2018;120:63902.
[25] Gao F, Xue H, Yang Z, et al. Topologically protected refraction of robust kink states in valley photonic crystals. Nat Phys 2018;14:140–4.
[26] Anderson PW. Absence of diffusion in certain random lattices. Phys Rev 1958;109:1492.
[27] Shi Z, Davy M, Genack AZ. Statistics and control of waves in disordered media. Opt Express 2015;23:12293–320.
[28] Schwartz T, Bartal G, Fishman S, Segev M. Transport and anderson localization in disordered two-dimensional photonic lattices. Nature 2007;446:52–5.
[29] Ong ZY, Lee CH. Transport and localization in a topological phononic lattice with correlated disorder. Phys Rev B 2016;94:134203.
[30] Orazbayev B, Kaina N, Fleury R. Chiral waveguides for robust waveguiding at the deep subwavelength scale. Phys Rev Appl 2018;10:54069.
[31] Lemoult F, Kaina N, Fink M, Lerosey G. Wave propagation control at the deep subwavelength scale in metamaterials. Nat Phys 2013;9:55–60.
[32] Colombi A, Roux P, Rupin M. Sub-wavelength energy trapping of elastic waves in a metamaterial. J Acoust Soc Am 2014;136:EL192.
[33] Kaina N, Causier A, Bourlier Y, Fink M, Berthelot T, Lerosey G. Slow waves in locally resonant metamaterials line defect waveguides. Sci Rep 2017;7:15105.
[34] Yves S, Fleury R, Lemoult F, Fink M, Lerosey G. Topological acoustic polaritons: robust sound manipulation at the subwavelength scale. New J Phys 2017;19:075003.
[35] Colombi A, Roux P, Guenneau S, Gueguen P, Craster RV. Forests as a natural seismic metamaterial: rayleigh wave bandgaps induced by local resonances. Sci Rep 2016;6:19238.
[36] Xiao D, Yao W, Niu Q. Valley-contrasting physics in graphene: magnetic moment and topological transport. Phys Rev Lett 2007;99:236809.
[37] Kariyado T, Hu X. Topological states characterized by mirror winding numbers in graphene with bond modulation. Sci Rep 2017;7:16515.
[38] Mulholland GW, Bohren CF, Fuller Ka. Light scattering by agglomerates: coupled electric and magnetic dipole method. Langmuir 1994;10:2533–46.
[39] Mott NF. Electrons in disordered structures. Adv Phys 1967;16:49–144.
[40] Goryachev M, Tobar ME. Reconfigurable microwave photonic topological insulator. Phys Rev Appl 2016;6:64006.
[41] Lemoult F, Kaina N, Fink M, Lerosey G. Soda cans metamaterial: a subwavelength-scaled phononic crystal. Crystals 2016;6:82.

Supplementary Material: The online version of this article offers supplementary material (https://doi.org/10.1515/nanoph-2019-0137).